

Size-Dependent Properties of Miura-ori Tessellations

C. Baek,¹ T. Tachi,² J. Yang,^{1,*} and H. Yasuda^{3,4,†}

¹*Department of Mechanical Engineering, Seoul National University, Seoul 08826, Republic of Korea*

²*Department of General Systems Studies, Graduate School of Arts and Sciences,
The University of Tokyo, Meguro-ku, Tokyo 153-8902, Japan*

³*Institute of Space and Astronautical Science, Japan Aerospace Exploration Agency, Sagami-cho, Kanagawa 252-5210, Japan*

⁴*Department of Aeronautics and Astronautics, University of Tokyo, Bunkyo-ku, Tokyo 113-8656, Japan*

(Dated: February 26, 2026)

We investigate the size-dependent behavior of Miura-ori-based origami tessellations by changing the number of origami unit cells. For large tessellations, the Miura-ori sheet generally exhibits a negative in-plane Poisson's ratio, whereas if the size of the Miura-ori tessellations becomes small, the transition between positive and negative Poisson's ratio emerges in the middle of the folding process. Here, we show that such a transitioning point, i.e., zero Poisson's ratio, yields a kinematic locking state. We also experimentally demonstrate the tunable locking behavior altered by tessellation sizes. Extending the analysis to three-dimensional origami tessellations, we find that the direction of kinematic locking changes depending on the tessellation size. Varying tessellation size thus enables control over both the onset and the direction of locking in origami metamaterials.

Size-dependent mechanical properties arise across materials science. Finite dimensions often constrain plastic flow and strengthen metals [1–3], while nominal strength and fracture depend on specimen size in composites [4–6]. Beyond conventional materials, architected metamaterials exhibit analogous size effects arising from geometry: stiffness and deformation depend on metrics such as a characteristic length or the number of unit cells. In many such systems, deformation localizes near free boundaries, causing bulk homogenization to fail when the structure comprises only a few unit cells [7–9].

Origami-based metamaterials, especially those stemming from rigid-foldable patterns such as the Miura-ori [10], provide a tractable platform for examining such geometry-property relations, as their mechanical response can often be expressed directly in geometric terms [11–14]. The Miura-ori possesses a single global degree of freedom (DOF) that persists across tessellation sizes, and its boundaries introduce no additional freedom, unlike systems where edge-localized modes drive finite-size effects [15, 16]. Of particular interest in engineering applications of origami is controlling the available DOFs to achieve structures that are foldable yet kinematically lockable. Prior studies typically induce locking through geometric heterogeneity or defects [12, 17], imposed symmetry [18], or panel self-contact [19, 20]. However, these approaches often restrict the accessible folding range and introduce localized effects, such as non-periodic mechanics or facet compliance beyond rigid-origami kinematics, complicating geometric descriptions of locking.

In this Letter, we demonstrate the onset of size-dependent, intrinsic locking in defect-free origami tessellations based on the Miura-ori. We show that the Poisson's ratio can switch between positive and negative values not only with the geometric parameters but also with the number of unit cells. At the zero-Poisson's-ratio transition, the structure exhibits kinematic lock-

ing. Although such kinematic locking in origami structures has been studied previously [21–23], the size effect of origami tessellations remains largely unexplored. Extending this finding to three-dimensional Miura-ori tube architectures reveals a broader mechanism: a quadratic form incorporating size-dependent Poisson's ratios governs directional locking across all tessellation scales and defines the locking-direction surface as an elliptic cone. Interestingly, for small tessellations, the cone's symmetry axis switches mid-folding; at the transition, two Poisson's ratios vanish, yielding anomalous locking directions described by intersecting planes.

We begin by defining the geometry of the Miura-ori. Figure 1(a) shows the unit cell of the Miura-ori, which consists of four identical parallelogram facets characterized by two side lengths, a and b , and an interior angle α . To describe the folded configuration, we use the folding parameter $\lambda = \sin \alpha \sin \theta_M$, where θ_M is the folding angle as shown in Fig. 1(a). Here, we define key dimensions of our unit cell (S , L , and V), expressed as

$$S = b\lambda, \quad L = \frac{a \cos \alpha}{\sqrt{1 - \lambda^2}}, \quad V = b\sqrt{1 - \lambda^2}. \quad (1)$$

To investigate the kinematics of the Miura-ori with different sizes (i.e., size effect), we consider the Miura-ori sheets composed of $N_x \times N_y$ unit cells [see Fig. 1(b) for $N_x = N_y = 4$ case]. The overall dimensions L_x and L_y are expressed in terms of the unit-cell parameters [Fig. 1(b)]:

$$L_x = 2N_x S, \quad (2)$$

$$L_y = 2N_y L + V. \quad (3)$$

Then, we obtain the in-plane infinitesimal Poisson's ratio defined by $\nu_{xy} = -(dL_y/L_y)/(dL_x/L_x)$, which gives

$$\nu_{xy} = -\frac{\cos \alpha - (b/a)(1 - \lambda^2)/(2N_y)}{\cos \alpha + (b/a)(1 - \lambda^2)/(2N_y)} \frac{\lambda^2}{1 - \lambda^2}. \quad (4)$$

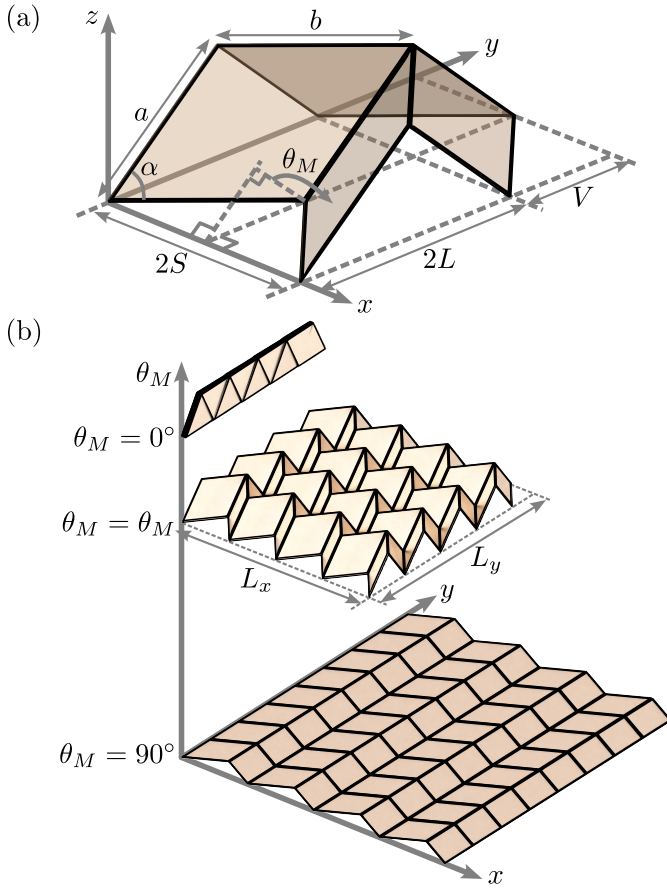


FIG. 1. Geometry of the Miura-ori. (a) Miura-ori unit cell. (b) Folding motion of 4×4 Miura-ori whose overall width and breadth are denoted by L_x and L_y , respectively.

Here, if we consider the bulk property when $N_y \rightarrow \infty$, the Poisson's ratio becomes $\nu_{xy} = -\lambda^2/(1 - \lambda^2)$ [12].

Figure 2 illustrates how the tessellation size N_y governs the Miura-ori kinematics. Note that throughout this study, we fix the unit-cell geometry ($\alpha = 70^\circ$, $b/a = 2$) for all analyses. Figure 2(a) shows the structural length L_y against λ/λ_{\max} for $N_y = 1$ (left) and $N_y = 3$ (right). Here, $\lambda_{\max} = \sin \alpha$. Our analysis reveals that the Miura-ori with $N_y = 1$ exhibits a non-monotonic shape change, whereas L_y varies monotonically for $N_y = 3$. For $N_y = 1$, L_y exhibits an interior minimum, which serves as a compression-stable equilibrium. Then, if the structure at such a minimum point is put under tension, the equilibrium is unstable and the motion bifurcates toward either the fully folded ($\lambda/\lambda_{\max} = 0$) or the fully deployed ($\lambda/\lambda_{\max} = 1$) state, depending on the perturbation direction [paths (i) and (ii) in Fig. 2(a, left)]. In contrast, for $N_y = 3$, no bifurcation occurs. This size dependence follows from Eq. (3): the tip length (V) is set solely by the unit-cell geometry [Fig. 1(a)], while the body part $2N_y L$ scales with N_y . These contributions vary oppositely with folding, and create an interior minimum in L_y for small

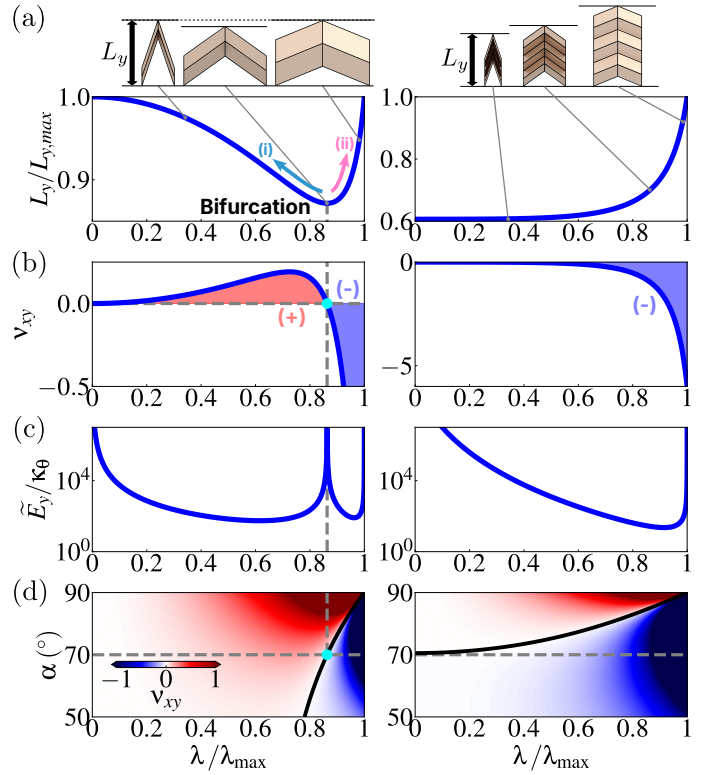


FIG. 2. Size-dependent behavior of the Miura-ori. We compare two Miura-ori tessellations with different sizes in the y direction: $N_y = 1$ (left) and $N_y = 3$ (right). For both cases, $N_x = 1$ and $(b/a, \alpha) = (2, 70^\circ)$. (a) Normalized length $L_y/L_{y,\max}$ versus λ/λ_{\max} ; insets show corresponding deployment sequences. (b) Poisson's ratio ν_{xy} versus λ/λ_{\max} . Red: positive, Blue: negative. (c) Nondimensionalized stiffness \tilde{E}_y/k_θ versus λ/λ_{\max} . (d) Colormaps of ν_{xy} in the $\alpha - \lambda/\lambda_{\max}$ plane; the black solid curve marks the locking trajectory.

N_y . As N_y increases, V becomes negligible and L_y becomes monotonic (see Supplemental Material [24]).

We also examine the Poisson's ratio ν_{xy} [Fig. 2(b)]. For $N_y = 1$, ν_{xy} is initially positive and becomes negative during unfolding. The sign change coincides with the interior minimum of L_y , as L_x is monotonic and $\nu_{xy} = -(dL_y/L_y)/(dL_x/L_x)$. In contrast, for $N_y = 3$, ν_{xy} remains negative throughout the entire folding range [12], consistent with the monotonic L_y and the absence of an interior extremum.

The Poisson's ratio can be linked to directional stiffness of the structure through the rigid-origami framework, where facets are modeled as rigid panels and creases as linear torsional springs with torsional stiffness per unit crease length, κ_θ . We introduce the nondimensionalized axial stiffnesses \tilde{E}_x and \tilde{E}_y , normalized by the cross-sectional area and structural length along the x and y axes, respectively. Since the Miura-ori is a one-degree-of-freedom mechanism, its in-plane strains depend on a single folding parameter, imposing the reciprocal symmetry $\nu_{xy} = 1/\nu_{yx}$ [25]. Together with the orthotropic

reciprocity condition $\nu_{xy}/\tilde{E}_x = \nu_{yx}/\tilde{E}_y$, this yields

$$\tilde{E}_y = \frac{\tilde{E}_x}{\nu_{xy}^2}. \quad (5)$$

Notice that \tilde{E}_y is not independent of \tilde{E}_x ; in this 1-DOF rigid-origami framework, all in-plane stiffnesses are kinematically coupled.

Figure 2(c) shows $\tilde{E}_y/\kappa_\theta$. For $N_y = 1$, \tilde{E}_y diverges at the mid-deployment state when $\nu_{xy} = 0$, as predicted by Fig. 2(a, b) and Eq. (5). From Eq. (4), the locking occurs when

$$\lambda = \sqrt{1 - \frac{2N_y}{(b/a)} \cos \alpha}. \quad (6)$$

This locking condition is physically admissible when $0 \leq \lambda \leq \sin \alpha$, equivalent to

$$\cos^{-1} \left[\min \left(\frac{(b/a)}{2N_y}, \frac{2N_y}{(b/a)} \right) \right] \leq \alpha \leq \frac{\pi}{2}. \quad (7)$$

Thus, the unit-cell geometry (α , b/a) and the tessellation size N_y jointly determine the locking behavior of the structure.

The size dependence is also evident in the colormaps of ν_{xy} against α and λ/λ_{\max} [Fig. 2(d)]. The solid black curve indicates $\nu_{xy} = 0$, i.e., the locking trajectory. For $N_y = 1$, a horizontal line at $\alpha = 70^\circ$ intersects this curve at $\lambda/\lambda_{\max} = 0.86$, which coincides exactly with the stiffness spike in Fig. 2(c, left), but not for $N_y = 3$ (see Fig. 2(c, right)).

To experimentally verify the locking behavior arising from the size effect, we fabricate prototypes and conduct uniaxial compression experiments. Miura-ori tubes are fabricated by joining two identical Miura-ori sheets made of 0.3 mm-thick SUS304H stainless-steel facets and fiber-reinforced tape hinges. All specimens share the identical unit-cell geometry. Figures 3(a) and (b) show a schematic and a photograph of the experimental setup, respectively. The force F_y is measured during compression using a load cell, while the in-plane kinematics (L_x , L_y) are tracked by digital image correlation. Also, a fitted rigid-origami model is used to compare our prediction with the experimental results. For the Miura-ori with $N_y = 1$ exhibiting kinematic bifurcation, we perform compression tests starting from two initial configurations: one from the unfolded side of the locking state and one from the folded side, as indicated by the arrows in Fig. 3(c). For the $N_y = 3$ specimen, the compression is applied only from the unfolded configuration, as shown in Fig. 3(d). See the Supplemental Material [24] for fabrication and fitting details; see Supplemental Movie S1 for uniaxial compression tests.

Figures 3(c) and (d) show the experimentally measured L_y and the theoretical prediction plotted against λ/λ_{\max} for $N_y = 1$ and $N_y = 3$, respectively. Figures 3(e) and

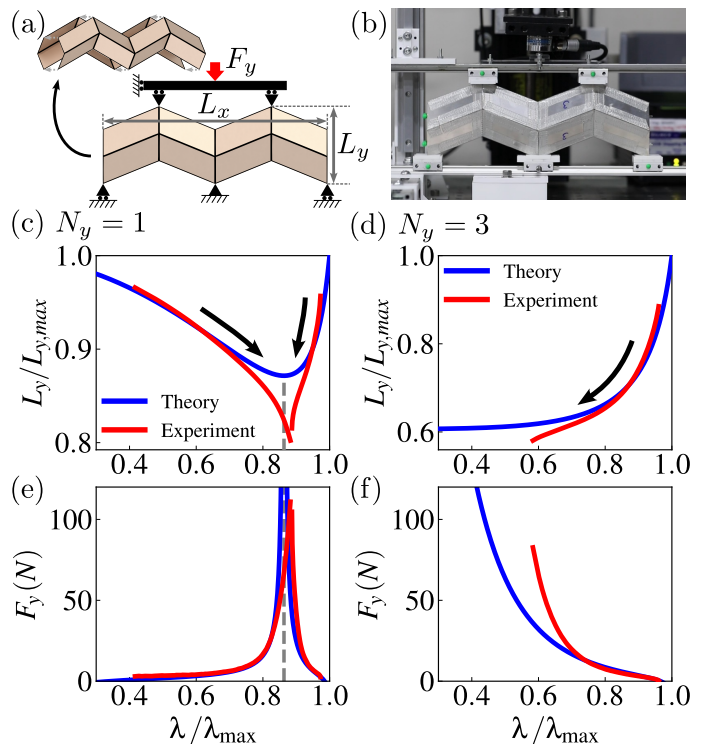


FIG. 3. Experimental validation of size-dependent locking in Miura-ori under uniaxial compression. (a) Mechanical boundary conditions. Inset: Miura-ori tube fabrication from two identical Miura-ori sheets. (b) Photo of the experimental setup. (c),(d) Comparison of theoretical and experimental mean normalized length $L_y/L_{y,max}$ versus λ/λ_{\max} for $N_y = 1, 3$; black arrows indicate the compression direction. (e),(f) Corresponding theoretical and experimental mean F_y - λ/λ_{\max} curves. Experimental curves show the mean of five trials; standard deviations are typically no larger than the line width and omitted for clarity. All samples share identical geometry with $\alpha = 70^\circ$, $b/a = 2$, and $N_x = 2$.

(f) present the measured and analytical axial force F_y for each case. For $N_y = 1$, both theory and experiment exhibit a non-monotonic L_y , producing a sharp spike in F_y near $\lambda/\lambda_{\max} = 0.86$ obtained from Eq. (6) [dashed line in Fig. 3(d)]. In contrast, for $N_y = 3$, L_y remains monotonic and compression drives the structure toward the fully folded endpoint, accompanied by a monotonic increase of F_y over the measured range. Despite facet deformation which allows L_y to drop below rigid-origami prediction and causes the force response to deviate at large compression, the overall trends confirm the size-dependent onset of a mid-deployment locking state.

The relation between Poisson's ratio and stiffness in the Miura-ori sheet suggests a broader principle: mid-deployment kinematic locking occurs when Poisson's ratio becomes zero. We further explore this principle in a three-dimensional Miura-ori tube by evaluating its response in any arbitrary direction. The 3D structure is formed by stacking identical Miura-ori sheets alternately

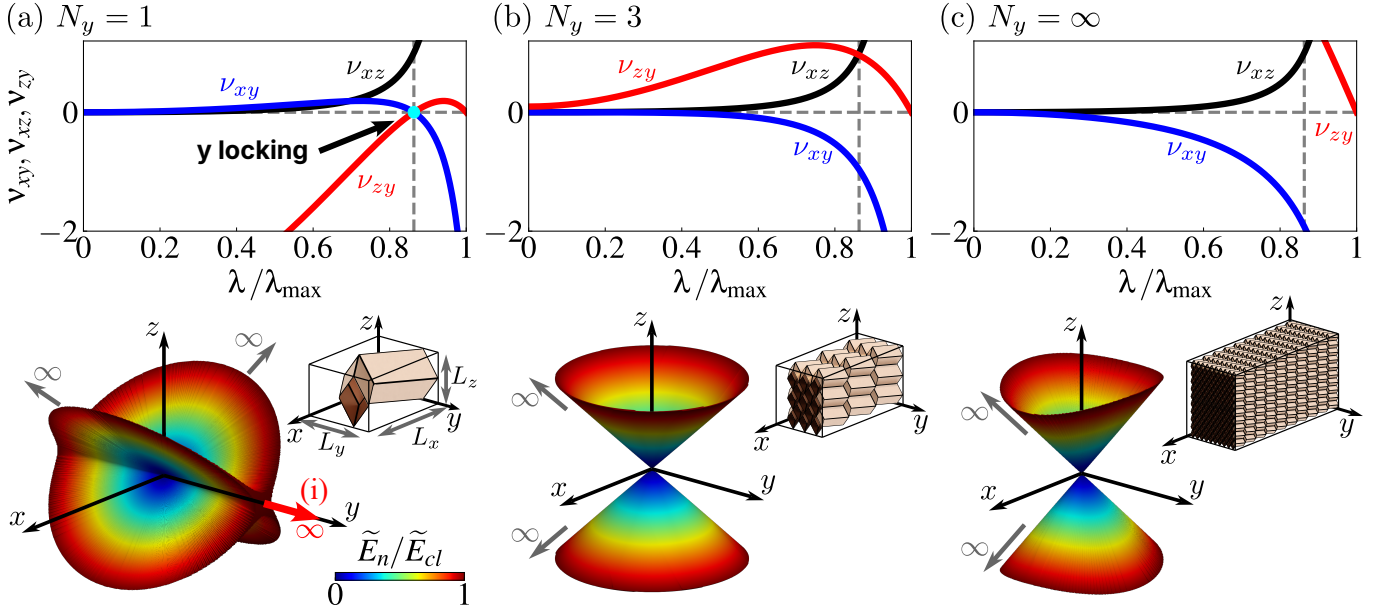


FIG. 4. Poisson's ratios and nondimensionalized stiffness of Miura-ori structures with different numbers of unit cells N_y and identical unit-cell geometry ($\alpha = 70^\circ$, $b/a = 2$). Poisson's ratios ν_{xy} , ν_{xz} , ν_{zy} are plotted as functions of λ/λ_{\max} . Insets show the nondimensionalized stiffness distributions \tilde{E}_n (diverging stiffness clipped at \tilde{E}_{cl} for visualization) and the rendered structures at $\lambda/\lambda_{\max} = 0.86$; color intensity indicates stiffness magnitude, and gray arrows mark representative directions on the divergence surfaces of \tilde{E}_n . All insets share a common coordinate system. (a) $N_y = 1$; arrow (i) indicates locking along the y axis. (b) $N_y = 3$; (c) $N_y \rightarrow \infty$.

flipped along the normal direction. The Poisson's ratios of the Miura-ori tube are ν_{xy} expressed by Eq. (4),

$$\nu_{xz} = \frac{\cos^2 \alpha}{\sin^2 \alpha - \lambda^2} \frac{\lambda^2}{1 - \lambda^2}, \quad (8)$$

and $\nu_{zy} = -\nu_{xy}/\nu_{xz}$ (see Supplemental Material [24]).

The nondimensionalized stiffness \tilde{E}_n along unit vector $n = (n_x, n_y, n_z)$ can be written solely using the kinematic properties and \tilde{E}_x [24]:

$$\tilde{E}_n = \frac{\tilde{E}_x}{(n_x^2 - \nu_{xy}n_y^2 - \nu_{xz}n_z^2)^2}. \quad (9)$$

This formulation provides a scale-independent measure of directional rigidity and recovers the conventional elastic modulus form in the large tessellation continuum limit. Also, Eq. (9) diverges, leading to kinematical locking, when

$$n_x^2 - \nu_{xy}n_y^2 - \nu_{xz}n_z^2 = 0. \quad (10)$$

It is noteworthy that the locking behavior of the Miura-ori tube can be characterized by a quadratic surface, and one of its coefficients, ν_{xy} , varies with tessellation size.

Figure 4 presents the Poisson's ratios as functions of λ/λ_{\max} for $N_y = 1, 3$, and ∞ , with identical unit-cell geometry. For $N_y = 1$, ν_{xz} is always positive in the entire folding range, whereas both ν_{xy} and ν_{zy} cross zero

at $\lambda/\lambda_{\max} = 0.86$ [Fig. 4(a)]. Here, the quadratic condition (Eq. (10)) defines an elliptic cone of locking directions, with its axis of symmetry along z (x) for $\nu_{xy} < 0$ ($\nu_{xy} > 0$) (see Supplemental Material [24] and Supplemental Movie S2 for the evolution of \tilde{E}_n as ν_{xy} changes sign). Interestingly, if ν_{xy} becomes zero, the cone degenerates into two planes $n_x = \pm\sqrt{\nu_{xz}}n_z$ intersecting along the y axis. The three-dimensional stiffness map at this point, computed from Eq. (9), diverges on the two predicted planes, with the y -directional locking highlighted by arrow (i) in Fig. 4(a). Although the Miura-ori sheet also locks in the y -direction (e.g., Fig. 2), its derivative (3D) tessellation exhibits richer locking capability in three-dimensional space.

In contrast, for $N_y = 3$ and $N_y \rightarrow \infty$ [Fig. 4(b), (c)], ν_{xy} and ν_{zy} do not cross zero mid-deployment. The stiffness maps at the same λ/λ_{\max} as in panel (a) are shown below for comparison. They show that \tilde{E}_n diverges on an elliptic cone without y -directional locking. Thus, we confirm that varying tessellation size selects the locking-direction surface and thereby activates or suppresses y -directional locking, demonstrating size-controlled programmability in origami-based structures. See Supplemental Movie S3 [24], which extends Fig. 4 by showing \tilde{E}_n at several λ/λ_{\max} values for $N_y = 1-10$.

In summary, we have investigated the size-dependent mechanical response of the origami tessellations based on the Miura-ori within the rigid-origami framework. For

small tessellations, finite-size effects create a local minimum in transverse width, resulting in zero Poisson's ratio. At this singular state, the axial stiffness diverges, yielding a mid-deployment locking state. On the other hand, as tessellation size increases, such locking behavior disappears. We further develop our analysis to three-dimensional Miura-ori tubes, where kinematic locking is characterized by a quadratic surface taking the shape of an elliptic cone. The size-dependent sign change of the Poisson's ratio reorients this locking surface; moreover, a zero crossing triggers a degeneracy into two planes, thereby activating locking along a principal axis. Thus, the locking of small Miura-ori sheets emerges as a special case of a broader Poisson-governed locking condition intrinsic to Miura-ori tubes. These results establish a unified geometric framework linking scale, kinematics, and anisotropy, enabling size-controlled programming of directional stiffness and locking.

Acknowledgments—We thank Yasuhiro Miyazawa for the discussions on experiments, Sunghyun Kim and Yubin Oh for help with metal fabrication. H.Y. gratefully acknowledges support from the JSPS KAKENHI JP22K18750. C.B. and J.Y. acknowledge the support from Air Force Office of Scientific Research (FA2386-24-1-4051), SNU-IAMD, SNU-IOER, and National Research Foundation grants funded by the Korean government [2023R1A2C2003705 and 2022H1D3A2A03096579].

Data Availability—The data are not publicly available. The data are available from the authors upon reasonable request.

* Corresponding author. Email: jkyang11@snu.ac.kr

† Corresponding author. Email: yasuda.hiromi@jaxa.jp

- [1] M. D. Uchic, D. M. Dimiduk, J. N. Florando, and W. D. Nix, Sample dimensions influence strength and crystal plasticity, *Science* **305**, 986 (2004).
- [2] N. Fleck, G. Muller, M. F. Ashby, and J. W. Hutchinson, Strain gradient plasticity: theory and experiment, *Acta Metallurgica et materialia* **42**, 475 (1994).
- [3] J. S. Stölken and A. Evans, A microbend test method for measuring the plasticity length scale, *Acta Materialia* **46**, 5109 (1998).
- [4] Z. P. Bažant, I. M. Daniel, and Z. Li, Size effect and fracture characteristics of composite laminates, *Journal of Engineering Materials and Technology* **118**, 317 (1996).
- [5] Z. P. Bažant and J. Planas, *Fracture and size effect in concrete and other quasibrittle materials* (Routledge, 2019).
- [6] S. Ko, J. Yang, M. E. Tuttle, and M. Salviato, Effect of the platelet size on the fracturing behavior and size effect of discontinuous fiber composite structures, *Composite Structures* **227**, 111245 (2019).
- [7] T. Frenzel, M. Kadic, and M. Wegener, Three-dimensional mechanical metamaterials with a twist, *Science* **358**, 1072 (2017).
- [8] C. Coullais, C. Kettenis, and M. van Hecke, A characteristic length scale causes anomalous size effects and boundary programmability in mechanical metamaterials, *Nature Physics* **14**, 40 (2018).
- [9] H. Yang and W. H. Müller, Size effects of mechanical metamaterials: a computational study based on a second-order asymptotic homogenization method, *Archive of Applied Mechanics* **91**, 1037 (2021).
- [10] K. Miura, Method of packaging and deployment of large membranes in space, The Institute of Space and Astronautical Science report , 1 (1985).
- [11] K. K. Dudek, M. Kadic, C. Coullais, and K. Bertoldi, Shape-morphing metamaterials, *Nature Reviews Materials* **10**, 783 (2025).
- [12] M. Schenk and S. D. Guest, Geometry of miura-folded metamaterials, *Proceedings of the National Academy of Sciences* **110**, 3276 (2013).
- [13] Z. Y. Wei, Z. V. Guo, L. Dudte, H. Y. Liang, and L. Mahadevan, Geometric mechanics of periodic pleated origami, *Physical review letters* **110**, 215501 (2013).
- [14] H. Yasuda and J. Yang, Reentrant origami-based metamaterials with negative poisson's ratio and bistability, *Phys. Rev. Lett.* **114**, 185502 (2015).
- [15] R. Imada and T. Tachi, Maxwell origami tube, *Physical Research* **7**, 013032 (2025).
- [16] B. G.-g. Chen, B. Liu, A. A. Evans, J. Paulose, I. Cohen, V. Vitelli, and C. D. Santangelo, Topological mechanics of origami and kirigami, *Physical review letters* **116**, 135501 (2016).
- [17] J. L. Silverberg, A. A. Evans, L. McLeod, R. C. Hayward, T. Hull, C. D. Santangelo, and I. Cohen, Using origami design principles to fold reprogrammable mechanical metamaterials, *science* **345**, 647 (2014).
- [18] X. Dang and G. H. Paulino, Axisymmetric blockfold origami: a non-flat-foldable miura variant with self-locking mechanisms and enhanced stiffness, *Proceedings of the Royal Society A* **480**, 20230956 (2024).
- [19] H. Fang, S. Li, and K. Wang, Self-locking degree-4 vertex origami structures, *Proceedings of the Royal Society A: Mathematical, Physical and Engineering Sciences* **472**, 20160682 (2016).
- [20] J. Gao and Z. You, Origami-inspired miura-ori honeycombs with a self-locking property, *Thin-Walled Structures* **171**, 108806 (2022).
- [21] T. Tachi and K. Miura, Rigid-foldable cylinders and cells, *Journal of the international association for shell and spatial structures* **53**, 217 (2012).
- [22] K. C. Cheung, T. Tachi, S. Calisch, and K. Miura, Origami interleaved tube cellular materials, *Smart Materials and Structures* **23**, 094012 (2014).
- [23] H. Yasuda, B. Gopalarethinam, T. Kunimine, T. Tachi, and J. Yang, Origami-based cellular structures with in situ transition between collapsible and load-bearing configurations, *Advanced Engineering Materials* **21**, 1900562 (2019).
- [24] See Supplemental Material at URL-will-be-inserted-by-publisher for additional kinematic derivations and geometric details, the rigid origami model, the compression experiment setup, and Supplemental Movies S1–S3.
- [25] K. Liu, P. P. Pratapa, D. Misseroni, T. Tachi, and G. H. Paulino, Triclinic metamaterials by tristable origami with reprogrammable frustration, *Advanced Materials* **34**, 2107998 (2022).
- [26] G. Bradski, The OpenCV Library, Dr. Dobb's Journal of Software Tools (2000).